



Article

Cow Dung-Based Biochar Materials Prepared via Mixed Base and Its Application in the Removal of Organic Pollutants

Xiaoxin Chen ^{1,2}, Gengxin Yu ^{1,2}, Yuanhui Chen ² , Shanshan Tang ^{1,2} and Yingjie Su ^{1,2,*}

¹ College of Life Sciences, Jilin Agricultural University, Changchun 130118, China

² Key Laboratory of Straw Comprehensive Utilization and Black Soil Conservation, Ministry of Education, Jilin Agricultural University, Changchun 130118, China

* Correspondence: yjsu@jlau.edu.cn

Abstract: Cow dung (CD) is a waste product of livestock production. Improper disposal of a large amount of CD will cause environmental pollution. In this work, three biochar materials based on CD (BMCD) were prepared by using three types of base, including KOH, NaOH, and mixed base (MB, a mixture of equal mass NaOH and KOH) as activators to investigate the different physicochemical properties of BMCDs (BMCD-K, BMCD-Na, and BMCD-MB). The objective was to verify the effectiveness of MB activation in the preparation of biochar materials. The results show that MB has an effect on the structural characteristics of BMCDs. In particular, the surface area and total pore volume, the specific surface area, and the total pore volume of BMCD-MB ($4081.1 \text{ m}^2 \text{ g}^{-1}$ and $3.0118 \text{ cm}^3 \text{ g}^{-1}$) are significantly larger than those of BMCD-K ($1784.6 \text{ m}^2 \text{ g}^{-1}$ and $1.1142 \text{ cm}^3 \text{ g}^{-1}$) and BMCD-Na ($1446.1 \text{ m}^2 \text{ g}^{-1}$ and $1.0788 \text{ cm}^3 \text{ g}^{-1}$). While synthetic dye rhodamine B (RhB) and antibiotic tetracycline hydrochloride (TH) were selected as organic pollutant models to explore the adsorption performances, the maximum adsorption capacities of BMCD-K, BMCD-NA and BMCD-MB were 951, 770, and 1241 mg g^{-1} for RhB, 975, 1051, and 1105 mg g^{-1} for TH, respectively, which were higher than those of most adsorbents. This study demonstrated that MB can be used as an effective activator for the preparation of biochar materials with enhanced performance.

Keywords: industrial wastewater; organic pollutants; cow dung; biochar materials; adsorption



Citation: Chen, X.; Yu, G.; Chen, Y.; Tang, S.; Su, Y. Cow Dung-Based Biochar Materials Prepared via Mixed Base and Its Application in the Removal of Organic Pollutants. *Int. J. Mol. Sci.* **2022**, *23*, 10094. <https://doi.org/10.3390/ijms231710094>

Academic Editor: Po-Hsiang Chang

Received: 17 August 2022

Accepted: 1 September 2022

Published: 3 September 2022

Publisher's Note: MDPI stays neutral with regard to jurisdictional claims in published maps and institutional affiliations.



Copyright: © 2022 by the authors. Licensee MDPI, Basel, Switzerland. This article is an open access article distributed under the terms and conditions of the Creative Commons Attribution (CC BY) license (<https://creativecommons.org/licenses/by/4.0/>).

1. Introduction

Industrial wastewater is one of the most acute causes affecting water safety [1]. Because it causes significant pollution, it not only threatens plants, animals and environment, but also poses a great danger to human health, so it has gradually become one a focal point for researchers [2–4]. Given this serious problem, various methods have been developed for the removal of organic pollutants (like antibiotics and dyes) from water, such as physical treatment including adsorption and reverse osmosis [5,6], and chemical treatment (using chemical reagents) including degradation and precipitation [7,8]. Among these methods, adsorption is widely used for wastewater treatment because of its environmental friendliness, low cost, and simple operation [5,9]. Normally, adsorbent is one of the most important factors affecting the effect of adsorption treatment and adsorption process. Biochar materials have found wide applications as adsorbents for the treatment of polluted wastewater due to their unique advantages, like high pore structure and large surface area [10,11]. To date, it is still necessary to explore new carbon resource of biochar materials in order to better cope with wastewater pollution treatment.

Cow dung (CD), a waste product of livestock production, is generally considered to be the undigested food residue of grazing animals (cattle) [12,13]. As cattle farming and cattle-feeding operations increase, so does the yield of the hard-to-handle waste CD. Since these waste emissions demonstrate a high risk of pathogen transmission, their disposal is considered a major challenge for the cattle and livestock industry [14,15]. In the past

decades, reports on comprehensive utilization of CD have emerged one after another. Because CD contains a large amount of undigested lignocellulose and inorganic salts, it is often used to produce bio-fertilizers, solid fuel, and friction composites, etc. [16,17]. With the progress of science and technology, only solving the problem of using waste CD is not enough to meet the development of society. Therefore, more and more researchers focus on how to use CD to produce high-performance products, to further improve its added value and release its economic potential. Recently, it has been demonstrated that CD-based biochar materials represented good porous structure and ideal surface area [18–20]. Obviously, this provides a new idea for many researchers, but how to further improve the performance of CD-based biochar materials remains a challenge.

Like many biochar materials, the biochar materials prepared by only carbonization have a low surface area and poor porosity, so further activation is required to improve their properties [21–24]. The selection and the number of different activators have significant influence on the porosity of the materials. Due to the different behaviors during activation, sodium hydroxide and potassium hydroxide are often used as activators for biochar materials. Over the past three years, our team constituted mixed base (MB) from equal masses of sodium hydroxide and potassium hydroxide, and have also been exploring the influence of MB on the preparation of biochar materials. Our previous studies have shown that the activation effect of MB on some biomass materials (such as corn straw, fungal hyphae, and edible fungus substrate) [21–24] may be better than that of the single base. However, there are few reports on whether the effect of preparing CD-based biochar materials with MB as activator is better than that of single base activation, which provides great motivation for us to explore this topic.

In this work, CD was used as raw material, after carbonization, three base including sodium hydroxide, potassium hydroxide, and MB were used as different activators for preparing CD-based biochar materials. The focus of this study is to explore the possibility of preparing CD-based biochar materials with enhanced performance via MB and the influence of different activators on the properties of biochar materials. Different characterization methods have been used to test the CD-based biochar materials in order to study the differences of physical and chemical structures of biochar materials with different activators. In addition, tetracycline hydrochloride (TH) and rhodamine B (RhB) were selected as organic pollutant models to explore the effects of different activators on the adsorption performances of CD-based biochar materials. This study aims to prepare a series of CD-based biochar materials with better performance. More importantly, this simple and efficient method can be further applied to produce other biochar materials.

2. Results and Discussion

2.1. Characterization Results

The change of CD with temperature under nitrogen protection was measured by TGA and DTG curves, and the results are shown in Figure S1. It can be seen that, with the increase of temperature, there are two obvious pyrolysis stages of CD. When the temperature is below 275 °C, the weight of the sample decreases slowly, which may be due to the evaporation of the water of crystal remaining in the sample as the temperature increases [25]. As the temperature continued to rise to 500 °C, the samples showed a dramatic weight loss, which could be explained by the high temperature decomposition of the oxygenated components of CD (fat, protein, and lignocellulose, etc.) into tar and combustible gases [26]. However, when the temperature exceeds 500 °C, the curve becomes stable without further weight loss, indicating that the carbonization process is complete. The trend of DTG curve was consistent with that of TGA curve, thus, the carbonization temperature was chosen as 500 °C.

The main component of CD is lignocellulose of straw or forage, and the results of SEM can show clear and obvious fiber structure (Figure 1B). With the completion of the carbonization process, the sample was dehydrated significantly (CDC), and the originally smooth fiber structure became wrinkled and broken (Figure 1C). Figure 1D–F shows the

morphological observation results of BMCDs prepared by different activators. It can be seen that all of them have drastic activation and fragmentation phenomenon, and the degree of fragmentation is different due to different activators. In particular, BMCD-MB is more severe. This is related to the activation efficiency of different activators, and also indicates the effectiveness of MB activation compared with single base under the same conditions.

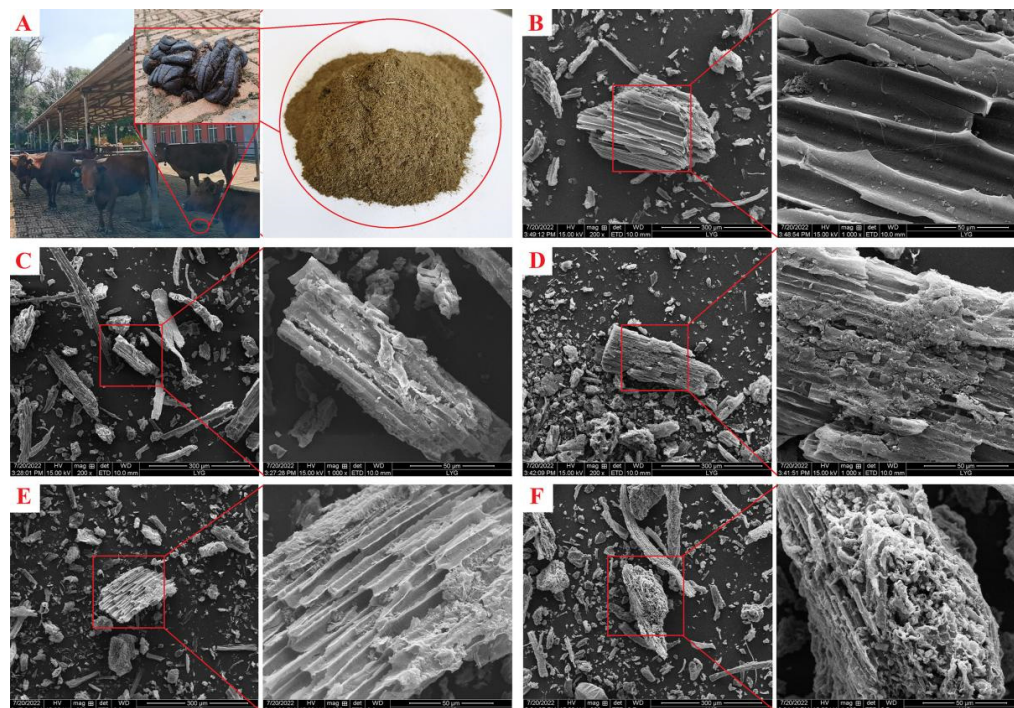


Figure 1. Digital photo of (A) CD. SEM images of (B) CD, (C) CDC, (D) BMCD-K, (E) BMCD-Na, and (F) BMCD-MB.

FT-IR were used to investigate the functional groups of the materials, and the results were shown in Figure 2A. The broadband corresponding to the -OH stretching vibration of hydroxyl functional groups in the range of $3450\text{--}3410\text{ cm}^{-1}$ is still existed, showing the existence of residual oxygen-containing functional groups on the resultant biochar materials [25,26]. The CDC and BMCDs had weaker -CH bonds ($2910\text{--}2930\text{ cm}^{-1}$, -CH group's symmetric and asymmetric stretching vibration peaks) than the CD, indicating that a considerable quantity of hydrogen was removed during the carbonization and activation procedures [27]. The aromatic ring's C=C stretching is indicated by the peak at 1619 cm^{-1} . This can be explained by the fact that the C-H bond may have decomposed into the more stable aromatic C=C bond after high-temperature preparation. This may be due to the conjugation of the C=O group to the aromatic ring and the formation of the carbonyl-containing group, which suggests that carbonyl-containing groups were formed during the aromatization process [28]. In addition, the overlapping bands in the $1000\text{--}1300\text{ cm}^{-1}$ region correspond to the stretching vibrations of the C-O and C-N heterocycles [27,28]. The characteristic peaks below 1100 cm^{-1} are mainly generated by the C-C skeleton vibrations, the bending vibrations of oxygen-containing groups (-CH, O-H), and the stretching vibrations of some single bonds (C-O, C-N) [28]. The presence of these large number of functional groups is likely to enhance the performance of BMCDs as adsorbents.

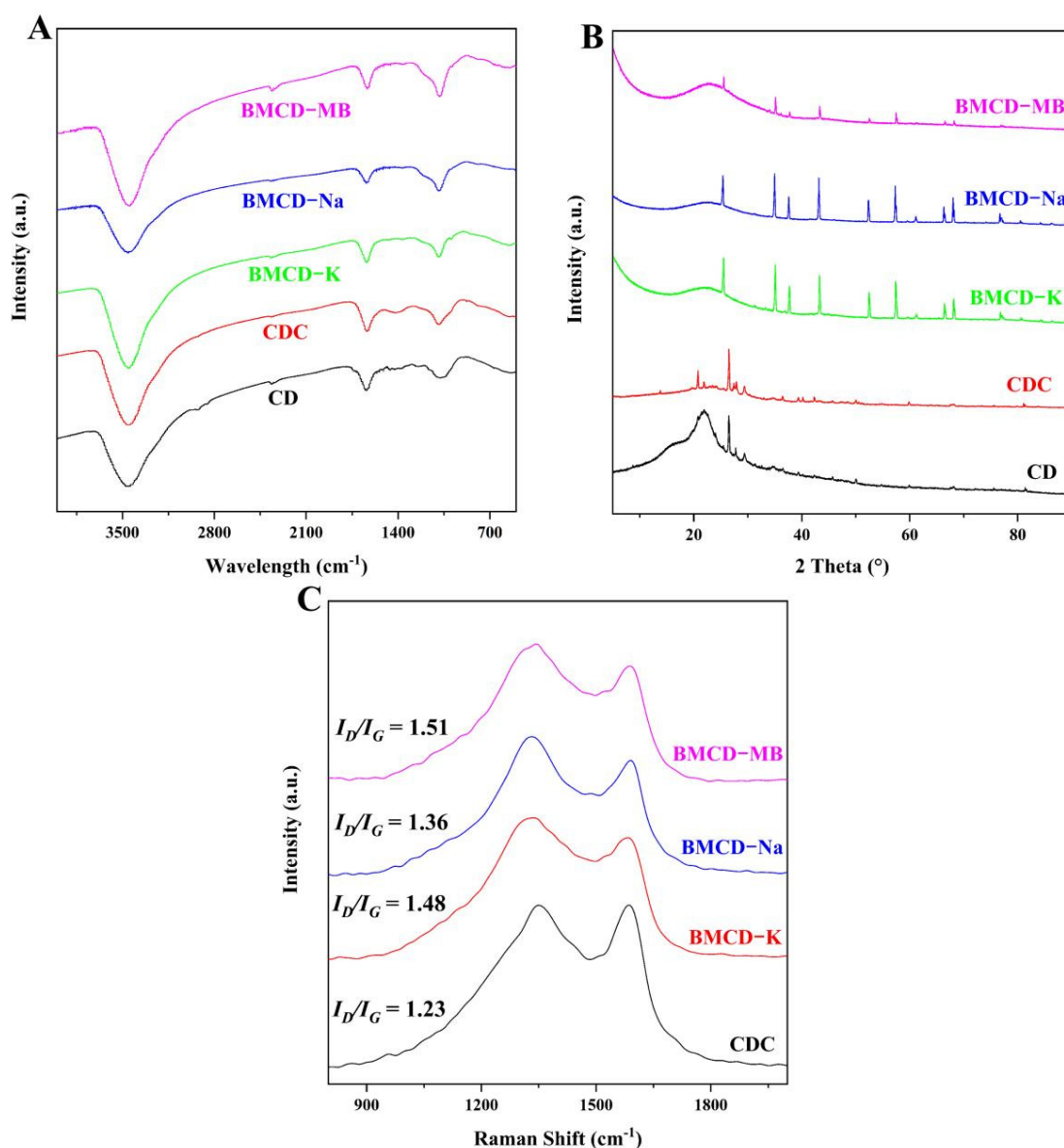


Figure 2. (A) FT-IR spectra, (B) XRD pattern, and (C) Raman spectra of biochar materials.

XRD were used to investigate the crystallinity in the carbons, and the results were shown as Figure 2B. The appearance peaks near 17° and 23° are due to the presence of a large amount of cellulose in the CD [29]. After carbonization (CDC) and activation (BMCDs), BMCDs still exhibited a diffraction peak within the range of 10° – 30° . This may be assigned to the plane of graphite structure (002), indicating that BMCDs had a classic local-order structure of carbon materials [9,11]. The intensity of this peak was weak and it was a broad peak, which can be explained by the fact that BMCDs contained both crystalline and amorphous structures [9,11]. Like many dung-based biochars [18,19], there are many irregular but distinct peaks, which can be explained by the inorganic salts (e.g., sodium chloride), bone meal, and shell meal, which were fed in the process of animal husbandry, connected to the carbon matrix during high temperature pyrolysis. However, there is no doubt that BMCDs were not crystalline but amorphous.

Raman tests were used to investigate the presence of defects in the biochar materials, the results were shown as Figure 2C. There were two typical peaks, the peak around $1330 \pm 25 \text{ cm}^{-1}$ is D-band associated with amorphous carbon and the G-band around $1550 \pm 30 \text{ cm}^{-1}$ is associated with graphitic carbon [30]. The intensity ratio of D-band (I_D) and G-band (I_G) (I_D/I_G) is an important parameter to measure the degree of

defect and disorder in carbons. The I_D/I_G values of BMCD-K, BMCD-Na, and BMCD-MB were 1.48, 1.36, and 1.51. Compared with the I_D/I_G values of CDC (1.23), the increase in BMCDs indicate the presence of more amorphous carbon structures generated in the biochar materials after activation [31].

N_2 adsorption-desorption isotherms were used to obtain the specific surface areas and porosity of the biochar materials, the results were shown as Figure 3 and Table 1. As can be seen from the inset of Figure 3A, the specific surface area and the total pore volume of CDC (23.8 $m^2 g^{-1}$, 0.0436 $cm^3 g^{-1}$) have been increased relative to that of CD (0.9 $m^2 g^{-1}$, 0.0071 $cm^3 g^{-1}$) after carbonization, which may be caused by high-temperature pyrolysis [25,26]. It is worth noting that CDC is not sufficient to support the excellent performance of CD-based on these results; thus, further activation is required to improve the specific surface area and pore volume.

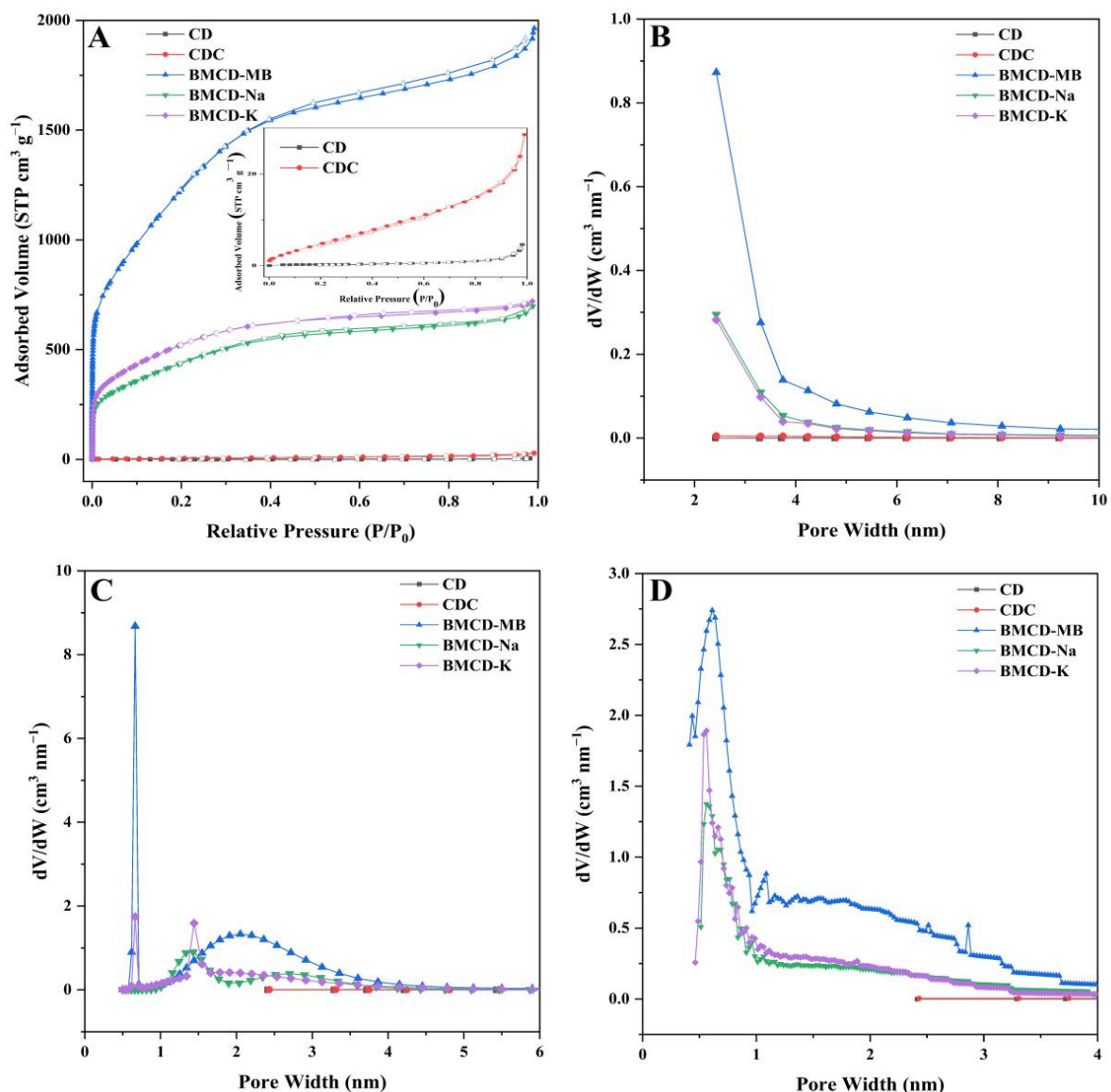


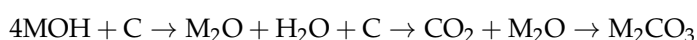
Figure 3. (A) N_2 adsorption-desorption isotherms of BMCD-K, BMCD-Na, and BMCD-MB (inset: N_2 adsorption-desorption isotherms of CD and CDC). Pore size distribution curves of CD, CDC, BMCD-K, BMCD-Na, and BMCD-MB based on (B) BJH, (C) NLDFT, and (D) H-K methods.

Table 1. The data of N₂ adsorption-desorption for BMCDs prepared via different activators.

Samples	S _{BET} (m ² g ⁻¹)	V _{micro} (cm ³ g ⁻¹)	P _m (nm)	V _{total} (cm ³ g ⁻¹)
CD	0.9	-	31.93	0.0071
CDC	23.8	-	7.34	0.0436
BMCD-K	1784.6	1.0239	2.50	1.1142
BMCD-Na	1446.1	0.9124	2.98	1.0788
BMCD-MB	4081.1	2.5583	2.95	3.0118

S_{BET} (m² g⁻¹) is the BET specific surface area, V_{micro} (cm³ g⁻¹) is the volume of micropores, P_m (nm) is the mean pore size, and V_{total} (cm³ g⁻¹) is the total pore volume.

After activation, the porosity of BMCDs were greatly improved. The specific surface areas of BMCD-K, BMCD-Na, and BMCD-MB were 1784.6, 1446.1, and 4081.1 m² g⁻¹. The total pore volume of BMCD-K, BMCD-Na, and BMCD-MB were 1.1142, 1.0788, and 3.0118 cm³ g⁻¹. All BMCDs displayed type I isotherms, showing the existence of a significant amount of micropores within the carbon compounds [29,31]. The volume of micropores of BMCD-K, BMCD-Na, and BMCD-MB were 1.0239, 0.9124, and 2.5583 cm³ g⁻¹, and they occupy 91.90%, 84.56%, and 84.94% of the total pore volume, respectively. Meanwhile, type IV hysteresis loops were discovered in all the samples' isotherms, although they were quite narrow, indicating that all of the samples included a modest quantity of mesopores [21,22]. According to the results of the pore distributions (Figure 3B–D), BMCDs were microporous materials containing mesoporous structures. Because micropores give adsorption sites and mesopores supply diffusion channels, the coexistence of micropores and mesopores favor adsorption. The possible mechanism of the activation is as follows (M represent the metal oxide in the base like Na in NaOH or K in KOH) [21–24]:



when MB was used as the activator, it was ionized into M⁺ and OH⁻ during high temperature pyrolysis. The reaction of MB with the precursor of the carbonized sample produced by-products such as carbon monoxide and hydrogen. While the hydrogen underwent chemical reactions to form water, the carbon monoxide reacted with water to form carbon dioxide. The carbon dioxide further reacted with the oxides generated by the MB to form carbonates that etched the carbonized sample. Finally, after washing with dilute acid and deionized water, the carbonates were removed to form microporous or mesoporous structures in the porous carbons.

XPS was performed to examine the surface chemistry and electronic state of the molecular of BMCDs. Like many biochars [32–34], BMCDs also contain mainly C, O, and N elements (Figure 4). The high-resolution C1s spectrum of the BMCDs showed four peaks, with the typical peaks at 283.91–284.15 eV corresponding to C-C, 285.23–285.69 eV corresponding to C-O, 286.82 eV corresponding to C=O, and 288.20 eV corresponding to O-C=C [25,26]. The high-resolution O1s spectrum of the BMCDs showed three peaks, with the typical peaks at 530.42 eV corresponding to quinones, 531.38 eV corresponding to C=O, 532.10–532.68 eV corresponding to C-O, and 534.13–534.79 eV corresponding to O-H [25,26]. The high-resolution N1s spectrum of the BMCDs showed two peaks, with the typical peaks at 398.08–399.52 eV corresponding to pyridinic-N and 400.10–400.95 eV corresponding to pyrrolic-N [33]. Moreover, interestingly, these functional groups are not significantly different despite the differences, which indicates that MB and its constituent single base do not significantly change their functional groups during activation. Besides, the above results, like FT-IR test results, once again indicate that the surface of BMCDs contains a large number of rich functional groups, which are likely to form hydrogen bonds with pollutant molecules during the adsorption process, thus enhancing the adsorption effect.

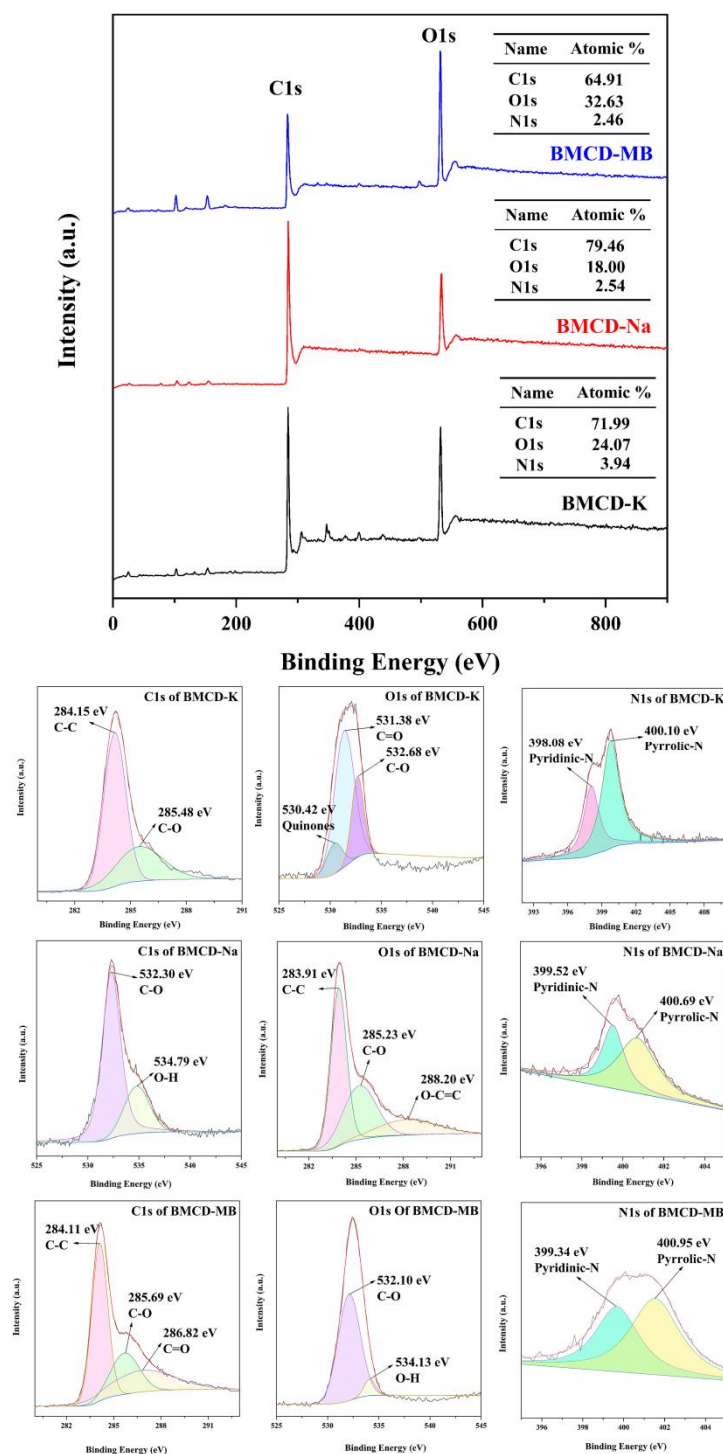


Figure 4. XPS spectra and the C1s, O1s, N1s of BMCD-K, BMCD-Na, and BMCD-MB.

Zeta potential test was used to evaluate the surface charges of BMCDs, and the results were shown as Figure 5. When pH changes from 2 to 10, the surface charges of BMCDs changes from positive (21.3, 17.3, and 17.6 for BMCD-MB, BMCD-K, and BMCD-Na) to negative (−32.4, −34.1, and −33.5 for BMCD-MB, BMCD-K, and BMCD-Na). Variable surface and constant charges determine the point at which the charge is zero, often referred to as the proton interaction charge density, the constant charge density, the charge density of the inner coordination complex, and the corresponding pH (pH_{pzc}), when the sum of the charge densities of the outer coordination complex is zero [35]. When the pH value is greater than pH_{pzc} , the sample surface is negatively charged, and vice versa. The pH_{pzc} of

all samples was less than the neutral value (7.00), indicating that BMCDs are more suitable for the treatment of cationic organic pollutants at higher pH [31]. Furthermore, the pH_{pzc} value of BMCD-MB is 4.62, which is between 4.48 of BMCD-K and 4.71 of BMCD-Na, indicating that different activators may have an effect on the preparation of biochars.

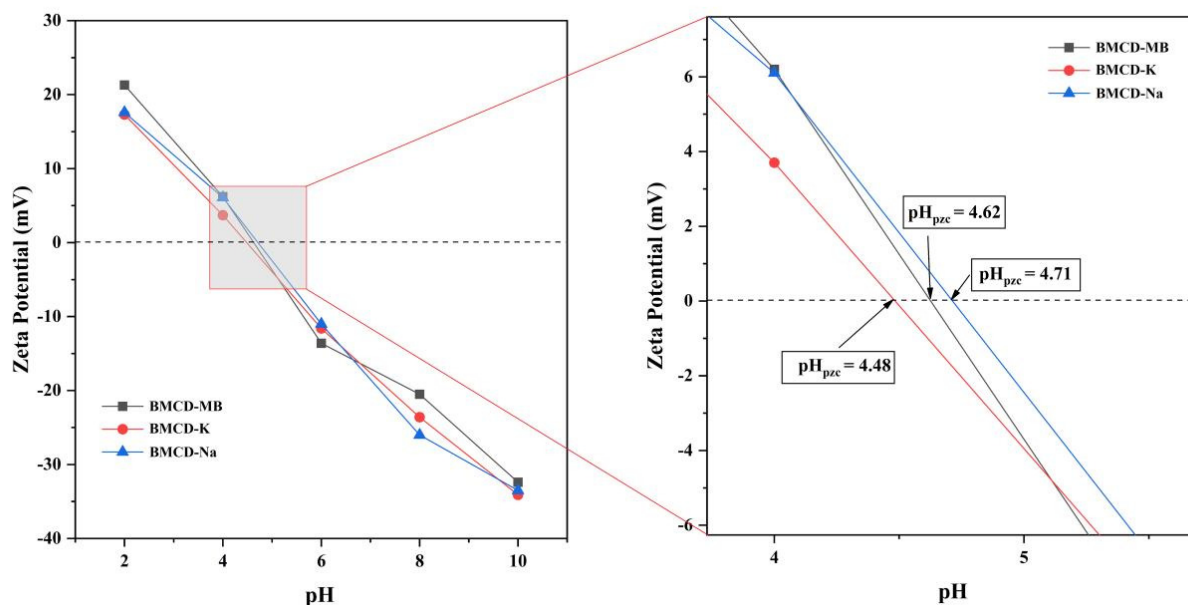


Figure 5. Zeta potential tests of BMCD-K, BMCD-Na, and BMCD-MB.

2.2. Adsorption Performances

2.2.1. Adsorption Kinetic

The adsorption kinetics describes the change of adsorbent with contact time, and is often used to study the influence of adsorbate concentration and the control mechanism of chemical reactions in the adsorption process [36–38]. The consequences of contact time on removal of RhB and TH (100, 200, and 300 mg L^{-1}) were shown as Figure 6A–C and Figure 6D–F by BMCD-K, BMCD-Na, and BMCD-MB. From these results, it can easily be found that no matter whether RhB or TH are adsorbed, all the adsorption curves have the same trend, that is, the adsorption capacity increases sharply in the first 5 min and gradually reaches the adsorption equilibrium in 60 min, which indicates that BMCDs have a rapid adsorption rate for removal of organic pollutants. In addition, the adsorption capacity increased significantly with the increase of adsorbate concentration, indicating that the higher solution concentration, the greater the adsorption capacity to some extent.

Herein, three adsorption kinetics models including the Pseudo-first-order kinetic, Pseudo-second-order kinetic, and the Intra-particle diffusion model were investigated, and the fitting parameters were shown in Table 2. The correlation coefficients (R^2) of the Pseudo-first-order kinetic were 0.9764–0.9930, 0.9523–0.9876, and 0.9559–0.9784 for BMCD-K, BMCD-K, and BMCD-MB while the adsorbate was RhB, 0.9703–0.9892, 0.9883–0.9907, and 0.9859–0.9913 while the adsorbate was TH, meanwhile, all the theoretical $Q_{e,cat}$ calculated according to the Pseudo-first-order kinetic model were lower than the Q_e obtained from the experiments, which indicates that the Lagergren's model probably did not play a significant role during the adsorption process [36]. While the adsorption data of RhB and TH were fitted to the Intra-particle diffusion model, the correlation coefficients (R^2) were 0.8205–0.9010 and 0.7407–0.8794 for BMCD-K, 0.7264–0.9135 and 0.7349–0.7626 for BMCD-Na, and 0.8164–0.9148 and 0.7467–0.8061 for BMCD-MB, meant that the Weber-Morris's model was not able to explain this adsorption process [37]. The Pseudo-second-order kinetic model was fitted to the adsorption data of BMCD-K, BMCD-Na, and BMCD-MB, and the correlation coefficients (R^2) were 0.9956–0.9988, 0.9963–0.9998, and 0.9904–0.9971 for RhB, and 0.9935–0.9998, 0.9990–0.9998, and 0.9989–0.9998 for TH, respectively. In

addition, the theoretical $Q_{e,cat}$ calculated according to the model were suitable with the experimental Q_e , demonstrated the applicability and potential dominance of Ho-McKay's model in the adsorption process [38]. Based on the above data, we can say that in the adsorption process of RhB and TH by BMCDs, the adsorption rate may be controlled by chemical reactions, and the similar reaction between adsorbent and adsorbate through transfer, exchange or sharing to form chemisorption bonds may promote the adsorption process.

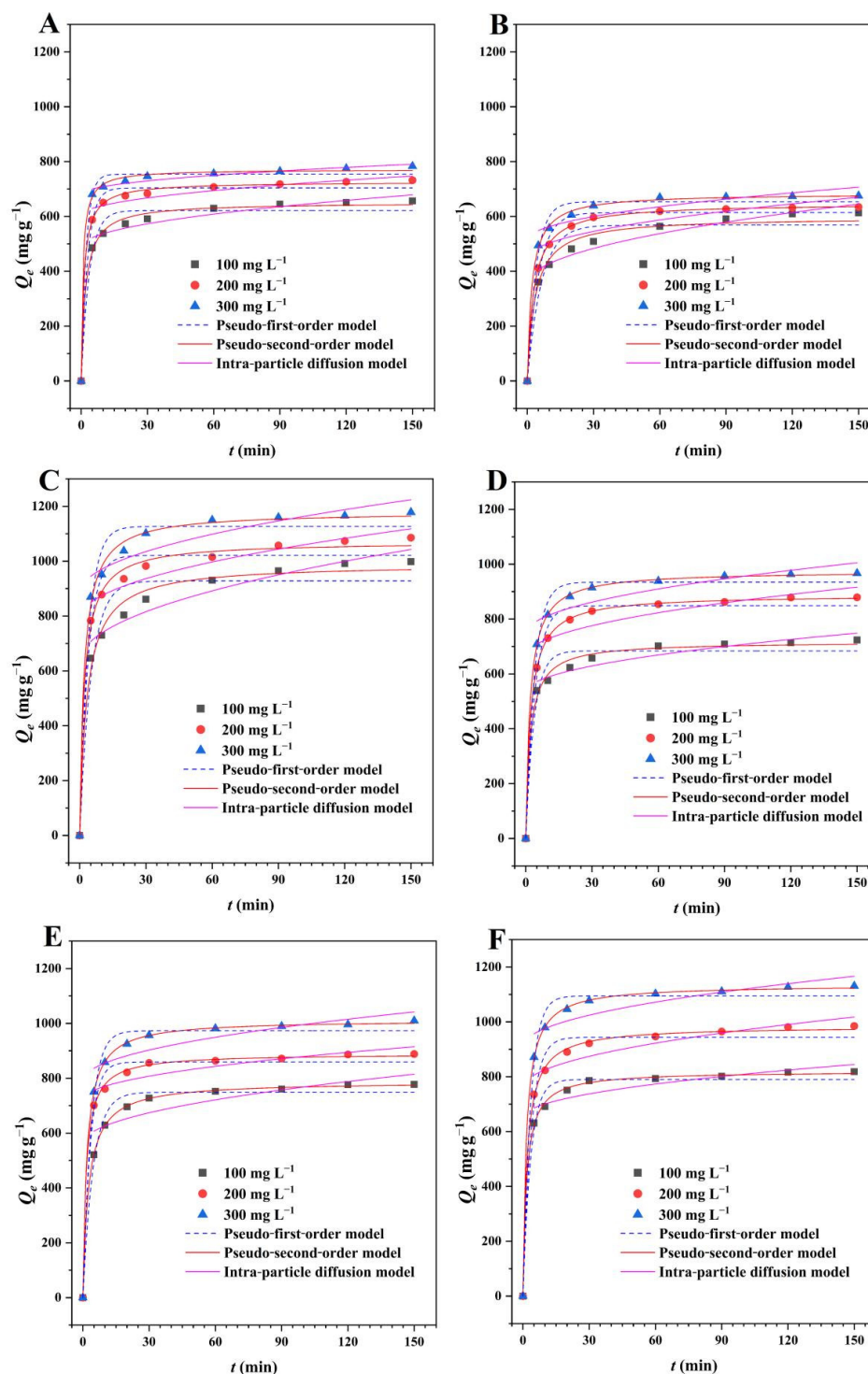


Figure 6. The adsorption kinetic plots of (A) BMCD-K, (B) BMCD-Na, and (C) BMCD-MB for RhB. The adsorption kinetic plots of (D) BMCD-K, (E) BMCD-Na, and (F) BMCD-MB for TH.

Table 2. Fitting parameters of adsorption kinetic models for RhB and TH at 303 K.

Organic Pollutants	Samples	Kinetic Models	Parameters	Concentration C_0 (mg L ⁻¹)			
				100	200	300	
RhB	BMCD-K	Pseudo-first-order	Q_e (mg g ⁻¹)	657	732	783	
			k_1 (min ⁻¹)	0.2704	0.3414	0.4440	
			$Q_{e.cat}$ (mg g ⁻¹)	622	704	754	
			R^2	0.9764	0.9914	0.9930	
		Pseudo-second-order	k_2 (g mg ⁻¹ min ⁻¹)	0.0007	0.0011	0.0017	
			$Q_{e.cat}$ (mg g ⁻¹)	661	736	791	
			R^2	0.9956	0.9988	0.9985	
			Intra-particle diffusion	k_3 (mg g ⁻¹ min ^{-0.5})	15.57	11.78	8.99
		C		488	586	680	
		R^2		0.8857	0.8205	0.9010	
		BMCD-Na		Pseudo-first-order	Q_e (mg g ⁻¹)	613	634
			k_1 (min ⁻¹)		0.1556	0.1948	0.2493
	$Q_{e.cat}$ (mg g ⁻¹)		569		614	654	
	R^2		0.9523		0.9876	0.9836	
	Pseudo-second-order		k_2 (g mg ⁻¹ min ⁻¹)	0.0004	0.0005	0.0007	
			$Q_{e.cat}$ (mg g ⁻¹)	617	648	684	
			R^2	0.9463	0.9998	0.9987	
			Intra-particle diffusion	k_3 (mg g ⁻¹ min ^{-0.5})	23.87	18.33	15.79
	C			353	445	513	
	R^2			0.9135	0.7264	0.7652	
	BMCD-MB			Pseudo-first-order	Q_e (mg g ⁻¹)	998	1086
			k_1 (min ⁻¹)		0.1916	0.2521	0.2593
		$Q_{e.cat}$ (mg g ⁻¹)	928		1021	1127	
		R^2	0.9559		0.9761	0.9784	
Pseudo-second-order		k_2 (g mg ⁻¹ min ⁻¹)	0.0003	0.0004	0.0005		
		$Q_{e.cat}$ (mg g ⁻¹)	999	1091	1180		
		R^2	0.9904	0.9956	0.9971		
		Intra-particle diffusion	k_3 (mg g ⁻¹ min ^{-0.5})	33.53	26.83	23.88	
C			632	790	882		
R^2			0.9148	0.8863	0.8164		
TH			BMCD-K	Pseudo-first-order	Q_e (mg g ⁻¹)	724	879
		k_1 (min ⁻¹)			0.2659	0.2399	0.2354
	$Q_{e.cat}$ (mg g ⁻¹)	684			849	935	
	R^2	0.9703			0.9891	0.9892	
	Pseudo-second-order	k_2 (g mg ⁻¹ min ⁻¹)		0.0006	0.0005	0.0005	
		$Q_{e.cat}$ (mg g ⁻¹)		727	888	975	
		R^2		0.9935	0.9998	0.9998	

Table 2. Cont.

Organic Pollutants	Samples	Kinetic Models	Parameters	Concentration C_0 (mg L ⁻¹)			
				100	200	300	
BMCD-Na	Intra-particle diffusion		k_3 (mg g ⁻¹ min ^{-0.5})	17.63	20.77	21.20	
			C	533	662	746	
			R^2	0.8794	0.7407	0.7497	
	Pseudo-first-order		Q_e (mg g ⁻¹)	778	888	1010	
			k_1 (min ⁻¹)	0.2138	0.3077	0.2705	
			$Q_{e.cat}$ (mg g ⁻¹)	749	859	973	
			R^2	0.9883	0.9889	0.9907	
			k_2 (g mg ⁻¹ min ⁻¹)	0.0005	0.0007	0.0005	
	Pseudo-second-order		$Q_{e.cat}$ (mg g ⁻¹)	788	890	1013	
			R^2	0.9998	0.9990	0.9998	
	Intra-particle diffusion		k_3 (mg g ⁻¹ min ^{-0.5})	20.77	15.83	15.52	
			C	560	720	791	
			R^2	0.7404	0.7626	0.7349	
	BMCD-MB	Pseudo-first-order		Q_e (mg g ⁻¹)	818	985	1131
				k_1 (min ⁻¹)	0.2886	0.2721	0.2940
$Q_{e.cat}$ (mg g ⁻¹)				790	944	1095	
R^2				0.9877	0.9859	0.9913	
Pseudo-second-order			k_2 (g mg ⁻¹ min ⁻¹)	0.0007	0.0006	0.0006	
			$Q_{e.cat}$ (mg g ⁻¹)	820	985	1135	
			R^2	0.9989	0.9990	0.9998	
Intra-particle diffusion		k_3 (mg g ⁻¹ min ^{-0.5})	15.83	21.17	20.94		
		C	651	758	910		
		R^2	0.7626	0.8061	0.7467		

2.2.2. Adsorption Isotherm

Adsorption isotherms are often used to study the effect of concentration on the adsorption capacity of an adsorbent and to illustrate how the adsorbent interacts with the adsorbate during adsorption [39–41]. The adsorption of different initiating concentrations of RhB and TH on BMCDs were investigated at 303 K (Figure 7) and the data were fitted using Langmuir and Freundlich isotherm models (Table 3). As the concentrations of RhB and TH increase, the adsorption capacities of BMCDs increased.

The correlation coefficients (R^2) were utilized to evaluate the experimental data and the results of the fit of the model equations. For RhB, the Langmuir correlation coefficients (R^2) were 0.9711, 0.7327, and 0.8807 for BMCD-K, BMCD-Na, and BMCD-MB; meanwhile, the Freundlich correlation coefficients (R^2) were 0.9854, 0.9823, and 0.9819. For TH, the Langmuir correlation coefficients (R^2) were 0.9595, 0.8885, and 0.9485 for BMCD-K, BMCD-Na, and BMCD-MB, simultaneously, the Freundlich correlation coefficients (R^2) were 0.9984, 0.9772, and 0.9933. In addition, it appears that the Freundlich isotherm model is more suitable for describing the adsorption process than the Langmuir isotherm model, suggesting that the adsorption process may not be homogeneous monolayer adsorption [39]. Furthermore, the intensity factors n_F of BMCD-K, BMCD-Na, and BMCD-MB related to the adsorption intensity or surface uniformity were 9.19, 8.77,

and 9.36 for RhB, 4.74, 4.81, and 4.56 for TH, which indicates that the adsorption process may involve multilayer adsorption on heterogeneous surfaces [39–41].

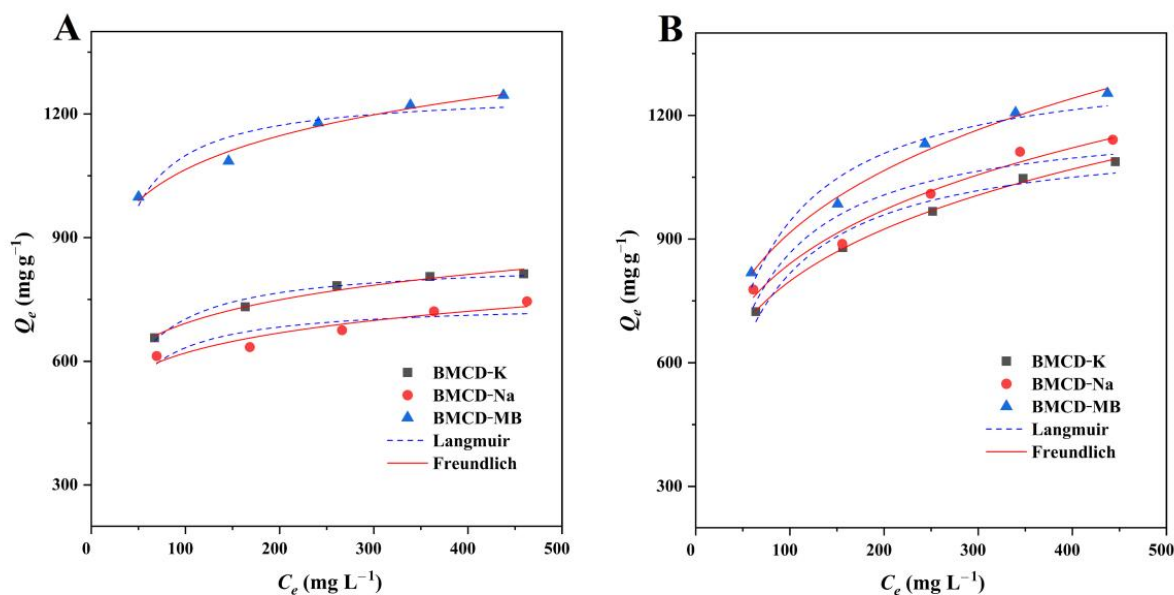


Figure 7. The adsorption isotherm plots of BMCD-K, BMCD-Na, and BMCD-MB for (A) RhB and (B) TH at 303 K.

Table 3. Fitting parameters of adsorption isotherm models for RhB and TH at 303 K.

Organic Pollutants	Samples	Isotherm Types	Parameters
RhB	BMCD-K	Langmuir	Q_m (mg g^{-1}) 843 K_L (L mg^{-1}) 0.0501 R^2 0.9711
		Freundlich	K_F ($\text{mg g}^{-1}(\text{L mg}^{-1})^{1/n}$) 376 n_F 9.19 R^2 0.9854
	BMCD-Na	Langmuir	Q_m (mg g^{-1}) 742 K_L (L mg^{-1}) 0.0580 R^2 0.7327
		Freundlich	K_F ($\text{mg g}^{-1}(\text{L mg}^{-1})^{1/n}$) 410 n_F 8.77 R^2 0.9823
	BMCD-MB	Langmuir	Q_m (mg g^{-1}) 1256 K_L (L mg^{-1}) 0.0703 R^2 0.8807
		Freundlich	K_F ($\text{mg g}^{-1}(\text{L mg}^{-1})^{1/n}$) 651 n_F 9.36 R^2 0.9819
TH	BMCD-K	Langmuir	Q_m (mg g^{-1}) 1161 K_L (L mg^{-1}) 0.0238 R^2 0.9595
		Freundlich	K_F ($\text{mg g}^{-1}(\text{L mg}^{-1})^{1/n}$) 302 n_F 4.74 R^2 0.9984

Table 3. Cont.

Organic Pollutants	Samples	Isotherm Types	Parameters	
	BMCD-Na	Langmuir	Q_m (mg g^{-1})	1203
			K_L (L mg^{-1})	0.0258
			R^2	0.8885
		Freundlich	K_F ($\text{mg g}^{-1}(\text{L mg}^{-1})^{1/n}$)	323
			n_F	4.81
			R^2	0.9772
BMCD-MB	Langmuir	Q_m (mg g^{-1})	1341	
		K_L (L mg^{-1})	0.0237	
		R^2	0.9485	
	Freundlich	K_F ($\text{mg g}^{-1}(\text{L mg}^{-1})^{1/n}$)	333	
		n_F	4.56	
		R^2	0.9933	

2.2.3. Adsorption Thermodynamic

Distinct temperatures (293, 303, and 313 K) had different effects on the adsorption capacities of the BMCDs on RhB and TH, the results were shown as Figure 8 and the parameters were shown in Table 4. The adsorption capacities of BMCD-K, BMCD-Na, and BMCD-MB for RhB were 762, 704, and 1140 mg g^{-1} , and 936, 1043, and 1154 for TH, respectively, at 293 K. As the temperature increased to 303 K, the adsorption capacities of BMCDs for RhB increased and that of TH followed the same pattern. When the temperature continues to increase further to 313 K, the increasing trend of adsorption capacities continues. Obviously, the increase of temperature promotes the adsorption process, i.e., a high-temperature environment is conducive to the adsorption of organic pollutants (RhB and TH) by BMCDs.

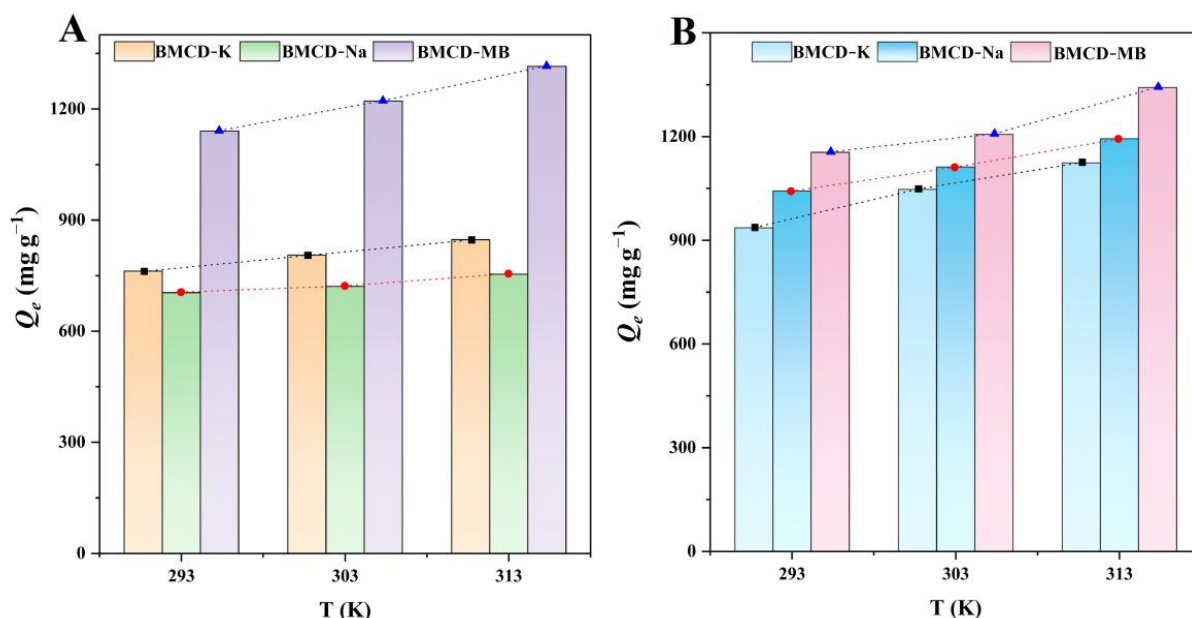


Figure 8. The adsorption thermodynamics of BMCD-K, BMCD-Na, and BMCD-MB for (A) RhB and (B) TH.

Table 4. Fitting adsorption thermodynamic parameters for RhB and TH.

Organic Pollutants	Samples	T (K)	ΔG (kJ mol ⁻¹)	ΔH (kJ mol ⁻¹)	ΔS (J mol ⁻¹ K ⁻¹)
RhB	BMCD-K	293	-1.81	4.49	21.51
		303	-2.03		
		313	-2.24		
	BMCD-Na	293	-1.60	2.87	15.27
		303	-1.72		
		313	-1.91		
	BMCD-MB	293	-2.93	6.41	31.86
		303	-3.23		
		313	-3.56		
TH	BMCD-K	293	-2.37	7.98	35.48
		303	-2.78		
		313	-3.08		
	BMCD-Na	293	-2.67	6.02	29.67
		303	-2.95		
		313	-3.27		
	BMCD-MB	293	-2.96	6.81	33.35
		303	-3.19		
		313	-3.63		

The ΔG values were all negative, suggesting that the adsorption happened spontaneously [25,26]. The standard enthalpy ΔH of BMCD-K, BMCD-Na, and BMCD-MB were counted as positive values (4.49, 2.87, and 6.41 kJ mol⁻¹ for RhB, 8.02, 6.02, and 6.81 kJ mol⁻¹ for TH), which further confirms the endothermic property ascribed to the adsorption process [25,26]. Moreover, the positive values of ΔS (21.51, 15.27, and 31.86 J mol⁻¹ K⁻¹ for RhB, 35.48, 29.67, and 33.35 J mol⁻¹ K⁻¹ for TH) showed an increase in the randomness of the interface between porous carbon and solution with increasing temperature [25,26].

2.2.4. The Effect of pH

pH is an important factor which has an effect on the surface properties of the adsorbent and on the chemical properties of the solution, and can promote or inhibit the adsorption capacity of the adsorbent [42]. The effect of pH change on the adsorption capacity was investigated by varying the pH of the solution in the range of 2–10, as shown in Figure 9. The cationic dye was electrostatically attracted to the adsorbent with a surface containing more negative charges as the pH increased from 2 to 10, increasing the adsorption capacity. When the pH was more than 6, no significant increase in adsorption capacity was found. TH was found in various forms at various pH levels. When the adsorbent surface is positively charged, it is present in the cationic form (TH⁺) below pH 3.30 [43]. This might result in electrostatic repulsion and a reduction in adsorption capacity. The adsorption capacity of pH values in the range 2–6 is larger, which might be attributed to an increase in the negative charge on the adsorbent surface and a decrease in the number of positive charges in the TH solution, strengthening the adsorbent's electrostatic attraction to TH [44]. The adsorption capacity continued to decrease as the pH increased to 10. TH was largely present in the form of anions (TH⁻ and TH²⁻) when the pH was greater than 7.68, and the substantial electrostatic repulsion with the negatively-charged adsorbent resulted in a drastic drop in the adsorption capacity [45].

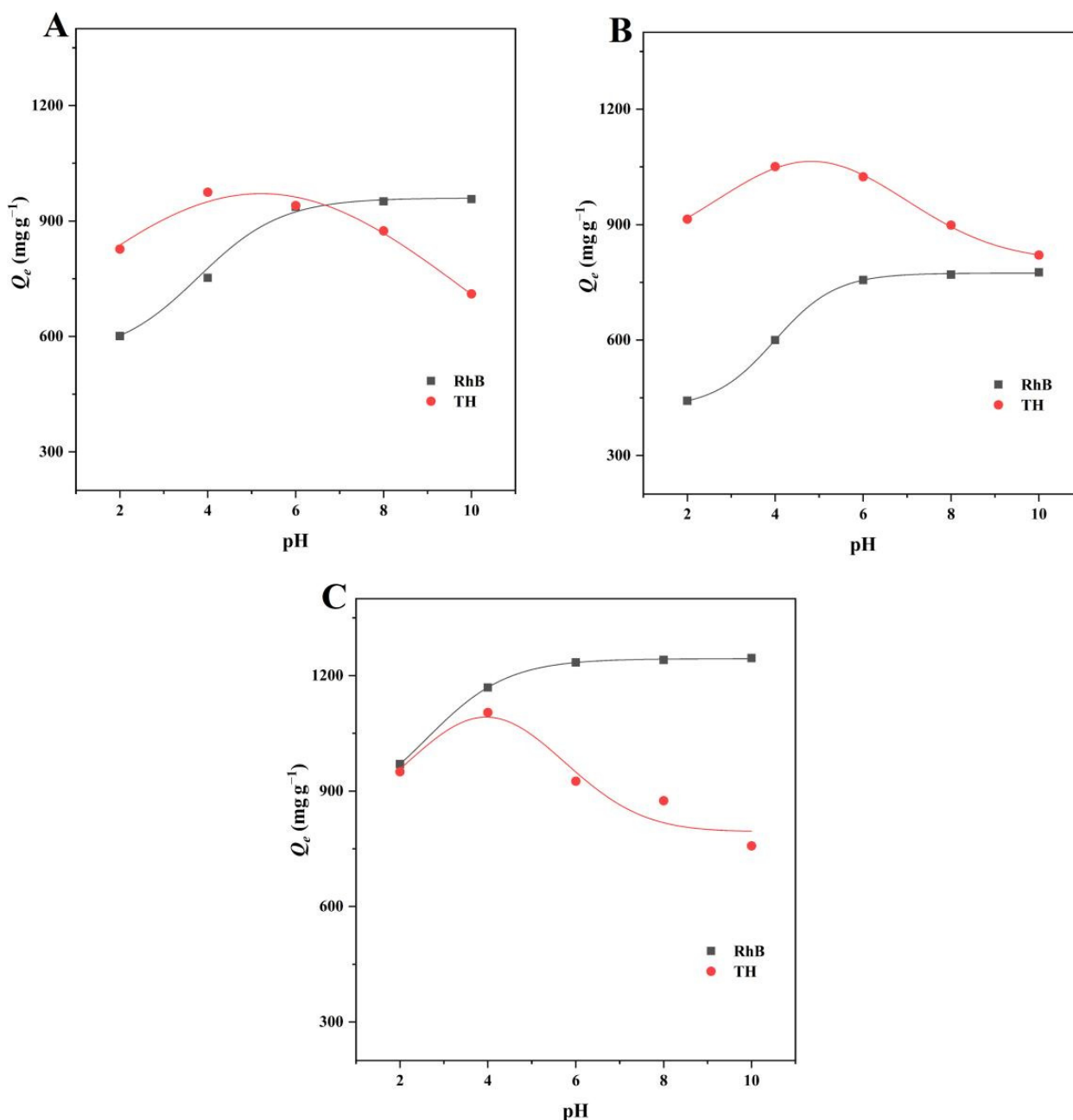


Figure 9. The effect of pH on the adsorption capacities of (A) BMCD-K, (B) BMCD-Na, and (C) BMCD-MB.

2.3. Reusability

In assessing the capacity of adsorbent materials, cycling stability is an important consideration. In this investigation, five cycle experiments were used to assess the regeneration capacities of the adsorbents. Figure 10 showed the number of cycles increased, the removal efficiency and adsorption capacity of regenerated BMCDs decreased. After 5 cycles, the removal efficiency and adsorption capacity of BMCD-K, BMCD-Na, and BMCD-MB could continue to maintain 81.5%, 82.4%, and 80.3% for RhB and 82.5%, 80.4%, and 80.5% for TH compared with original BMCDs, which indicates reasonable regeneration capability and reusability.

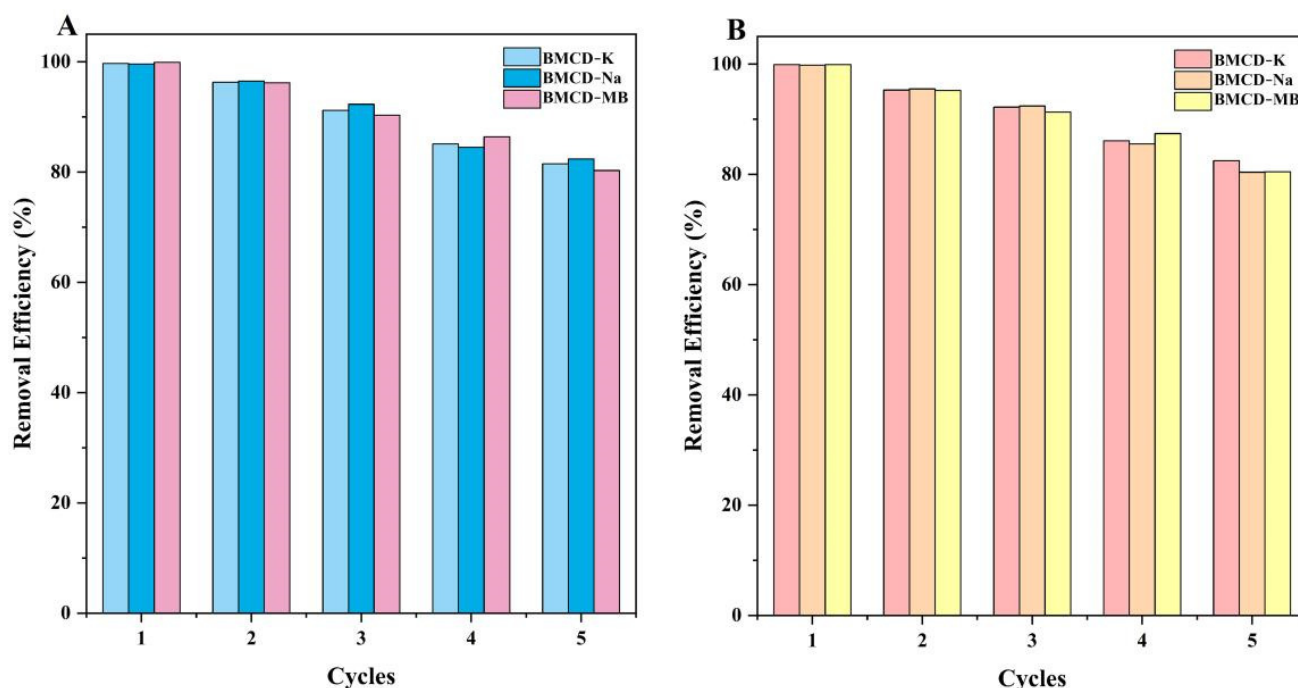


Figure 10. Reusability of the BMCD-K, BMCD-Na, and BMCD-MB for (A) RhB and (B) TH.

2.4. The Probable Adsorption Mechanism

In this study, the adsorption mechanisms that may affect the excellent adsorption performance of BMCDs mainly include pore filling, π - π interaction, H-bond interaction, and electrostatic attraction (Figure 11). The large surface areas (1784.6, 1446.1, and 4081.1 $\text{m}^2 \text{g}^{-1}$) and high pore volumes (1.1142, 1.0788, and 3.0118 $\text{cm}^3 \text{g}^{-1}$) of BMCD-K, BMCD-Na, and BMCD-MB provide a large number of adsorption sites, besides, the mean pore width (2.50, 2.98, and 2.95 nm) of BMCDs were larger than that of the molecular size of RhB (1.2 nm) and TH (1.3 nm), so it can be speculated that pore filling may play a dominant role in the adsorption processes. Strong electrostatic interaction exists between the organic pollutants and BMCDs with a negative zeta potential, resulting in greater adsorption capacity at higher pH aqueous environment. The presence of various functional groups on these adsorption sites that are beneficial for adsorption, such as C=O groups that may form H-bonds with the C-H groups in organic pollutants, can be seen using FT-IR spectrum data and XPS analysis findings. The results of FT-IR spectroscopy and Raman tests reveal the existence of aromatic rings in the BMCDs, which might result in π - π interactions with the aromatic rings in organic pollutants, enhancing adsorption capacities.

Besides, in the solutions of 400 mg L^{-1} at 303 K, the adsorption capacities of BMCD-K, BMCD-Na, and BMCD-MB were 951, 770, and 1241 mg g^{-1} for RhB, and 975, 1051, and 1105 mg g^{-1} for TH, respectively, which are significantly better than for most other adsorbents (Tables S1 and S2), indicating that BMCDs have great potential for removal of organic pollutants from aqueous media.

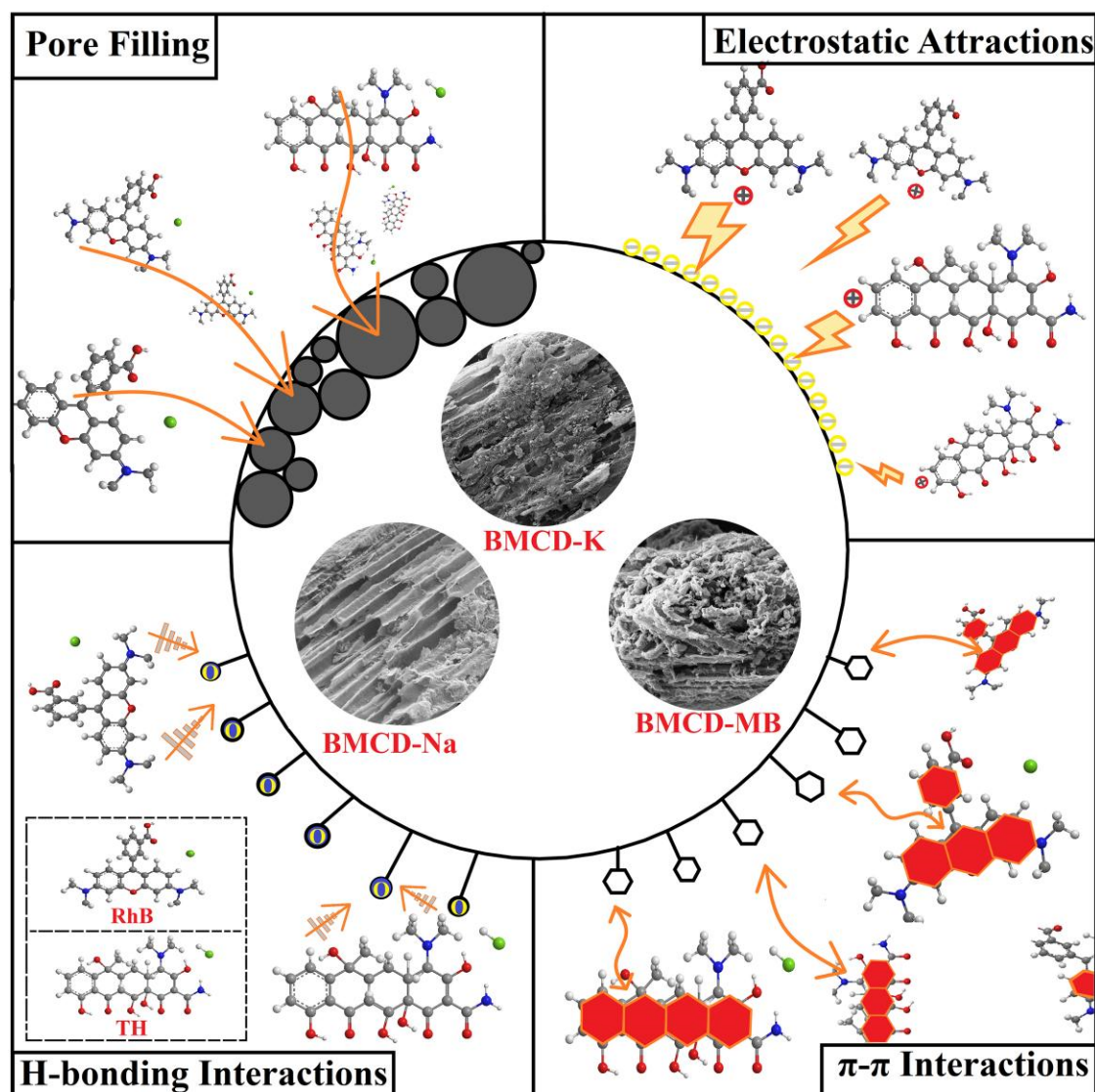


Figure 11. The probable adsorption mechanism diagram of BMCD-K, BMCD-Na, and BMCD-MB to RhB and TH.

3. Materials and Methods

3.1. Materials and Reagents

Cow dung (CD) was provided by the cattle farm of the Jilin Academy of Agricultural Sciences.

HCl, KOH, and NaOH were supplied by Beijing Chemical Works (Beijing, China). Tetracycline hydrochloride (TH) and Rhodamine B (RhB) were supplied by Aladdin Chemical (Shanghai) Co., Ltd. (Shanghai, China) and the structural formulas of RhB and TH were shown as Figure S2 (Supporting Information). Mixed base (MB) was a mixture of equal mass NaOH and KOH. All the above reagents were of analytical purity grade and did not require further purification. The water involved in the rinsing and preparation process was deionized water.

3.2. Preparation of Cow Dung-Based Biochar Materials

The CD after carbonization is referred to as CDC. After carbonization, 2 g of activators (KOH, NaOH and MB) were used to grind 0.5 g of CDC adequately. The combined samples were heated to 700 °C at 10 °C min⁻¹ in a horizontal tube furnace and kept for 90 min under nitrogen atmosphere. The activated samples were then rinsed with hydrochloric acid

and ultrapure water until they had pH = 7. Samples were collected and dried at 120 °C for 12 h, then stored in desiccators. The CD-based biochar materials (BMCDs) activated with KOH, NaOH and MB were referred to as BMCD-K, BMCD-Na, and BMCD-MB.

3.3. Adsorption Experiments

The adsorption properties of the samples were studied using RhB and TH as organic pollutants. In equilibrium adsorption experiments, 10 mg of BMCDs was added to a flask containing 200 mL solutions. The flask was placed in a constant temperature shaker with speed of 150 rpm, and the suspension was subsequently centrifuged. After that, 1 mL of supernatant was taken and diluted with 99 mL deionized water. The concentration of the solution was determined by UV-vis spectrophotometer (Agilent Cary300, Stockton, CA, USA) at selected wavelengths (554 nm for RhB and 357 nm for TH). The standard curves of RhB and TH were shown in Figure S3. The adsorption capacities of the samples were calculated by Equation (1):

$$Q_e = \frac{(C_0 - C_e) \times V}{m} \quad (1)$$

where Q_e (mg g⁻¹) is the adsorption capacity of porous carbon, C_e and C_0 (mg L⁻¹) denote the equilibrium and initial concentrations of the dye solution. m (g) and V (L) denote the mass of the adsorbent and the volume of the solution, respectively.

3.3.1. Adsorption Kinetic Experiments

The contaminant solutions were prepared at different concentrations (100, 200, and 300 mg L⁻¹). A quantity of 10 mg of BMCDs was dispersed into flasks containing 200 mL solutions and shaken at 150 rpm on a constant temperature shaker. Then the concentrations of the solutions were determined at preset time intervals.

The adsorption kinetic models including the Pseudo-first-order kinetic Equation (2), Pseudo-second-order kinetic Equation (3), and the Intra-particle diffusion model Equation (4) were used to calculate the adsorption rate constants. The models are expressed below:

$$Q_t = Q_e \left(1 - e^{-k_1 t}\right) \quad (2)$$

$$Q_t = \frac{k_2 Q_e^2}{(1 + k_2 Q_e t)} t \quad (3)$$

$$Q_t = k_3 t^{0.5} + C \quad (4)$$

where k_1 , k_2 , and k_3 represent the rate constants of the kinetic models, respectively, Q_t is the adsorption capacity of a sample at different time points, and C represents the constant of the boundary layer thickness.

3.3.2. Adsorption Isotherm Experiments

The contaminant solutions at different initial concentrations (100, 200, 300, 400, and 500 mg L⁻¹) were prepared and used to test the adsorption isotherm at 303 K. The absorbances of the solutions were measured after adsorption saturation. The adsorption isotherm models including Langmuir Equation (5) and Freundlich Equation (6) isotherm models were used to investigate the possible adsorption mechanisms. The isotherm models are expressed below:

$$Q_e = \frac{Q_m K_L C_e}{1 + K_L C_e} \quad (5)$$

$$Q_e = K_F C_e^{\frac{1}{n_F}} \quad (6)$$

where Q_m (mg g⁻¹) represents the maximum adsorption capacity of a sample, C_e (mg L⁻¹) is the solution concentration at equilibrium, K_L and K_F represent the constants of the

Langmuir and Freundlich models, respectively. n_F represent the constants of the Freundlich isotherm models.

3.3.3. Adsorption Thermodynamic Experiments

The effect of temperature on the adsorption capacity of the adsorbate was investigated at an initial concentration of 400 mg L⁻¹. The thermodynamic parameters standard entropy (ΔS), standard free Gibbs energy (ΔG), and standard enthalpy (ΔH) were analyzed to describe the effect of temperature on the adsorption process. The relationship between ΔH , ΔS , and ΔG could be calculated by using the following Equations (7) and (8):

$$\ln\left(\frac{Q_e}{C_e}\right) = \frac{\Delta S}{R} - \frac{\Delta H}{RT} \quad (7)$$

$$\Delta G = \Delta H - T\Delta S \quad (8)$$

where T is the temperature (K), and R represents the gas constant (8.314 JK⁻¹ mol).

3.3.4. The Effect of pH on Adsorption Capacities

The variation of the adsorption capacity of the samples with pH (2, 4, 6, 8, and 10) was also investigated. The solutions were adjusted to different pH values by HCl and NaOH. After adsorption saturations were achieved, the adsorption capacities of the samples were calculated.

3.4. Reusability Studies

The economic efficiencies of the adsorbents were assessed by their cycling performances. A quantity of 0.1 g of BMCDs was placed into 100 mL of contaminants in each cycle (200 mg L⁻¹). After adsorption, the recycled carbon was centrifuged. Following this, the BMCDs were washed with water, dried, and carbonized for 60 min at 500 °C under N₂ protection. In the next cycle, these samples were employed as fresh adsorbents.

The details of characterization methods were shown as S1 in Supporting Information.

4. Conclusions

In this work, CD was used as raw material, and NaOH, KOH, and MB were used as activators to prepare biochar materials. This work not only confirmed the different effects of NaOH and KOH in the activation process, but also verified the higher efficiency of MB and prepared CD-based biochar materials with higher performance. The specific surface area and the total pore volume of BMCD-MB (4081.1 m² g⁻¹ and 3.0118 cm³ g⁻¹) are significantly larger than those of BMCD-K (1784.6 m² g⁻¹ and 1.1142 cm³ g⁻¹) and BMCD-Na (1446.1 m² g⁻¹ and 1.0788 cm³ g⁻¹). While the synthetic dye RhB and antibiotic TH were used as organic pollutants models, the maximum adsorption capacities of BMCD-K, BMCD-Na, and BMCD-MB were 951, 770, and 1241 mg g⁻¹ for RhB, and 975, 1051, and 1105 mg g⁻¹ for TH, respectively. Furthermore, the adsorption capacities of BMCDs to RhB and TH can still be over 80% after 5 cycles. This work not only prepared a series of biochar materials (BMCDs) with enhanced performance, which can better cope with organic pollutants wastewater treatment, but more importantly, it provided a new strategy for the exploration of other biomasses. In the future, we will continue to explore the types and uses of MB in depth to further explore the activation potential of MB.

Supplementary Materials: The supporting information can be downloaded at: <https://www.mdpi.com/article/10.3390/ijms231710094/s1>. References [22,46–74] are cited in the supplementary materials.

Author Contributions: Conceptualization, X.C.; Formal analysis, S.T.; Funding acquisition, Y.S.; Investigation, G.Y.; Methodology, S.T.; Project administration, Y.C. and Y.S.; Supervision, Y.S.; Validation, G.Y.; Visualization, Y.C.; Writing—original draft, X.C. All authors have read and agreed to the published version of the manuscript.

Funding: This research was funded by [Jilin Scientific and Technological Development Program] grant number [20220203108SF] and [Education Department of Jilin Province] grant number [JJKH20210323KJ]. The APC was funded by [20220203108SF].

Institutional Review Board Statement: The study did not require ethical approval.

Informed Consent Statement: Not applicable.

Data Availability Statement: The study did not report any data.

Acknowledgments: Thanks for the supporting by Xiqing Wang (College of Food Science Technology and Chemical Engineering, Hubei University of Arts and Science) in this work.

Conflicts of Interest: The authors declare no conflict of interest.

References

1. Singh, A.; Srivastava, A.; Saidulu, D.; Gupta, A.K. Advancements of sequencing batch reactor for industrial wastewater treatment: Major focus on modifications, critical operational parameters, and future perspectives. *J. Environ. Manag.* **2022**, *317*, 115305. [[CrossRef](#)] [[PubMed](#)]
2. Liu, M.; Lv, J.; Qin, C.; Zhang, H.; Wu, L.; Guo, W.; Guo, C.; Xu, J. Chemical fingerprinting of organic micropollutants in different industrial treated wastewater effluents and their effluent-receiving river. *Sci. Total Environ.* **2022**, *838*, 156399. [[CrossRef](#)] [[PubMed](#)]
3. Kim, S.Y.; Park, J.W.; Noh, J.H.; Bae, Y.H.; Maeng, S.K. Potential organic matter management for industrial wastewater guidelines using advanced dissolved organic matter characterization tools. *J. Water Process Eng.* **2022**, *46*, 102604. [[CrossRef](#)]
4. Charazinska, S.; Lochynski, P.; Markiewicz, M.; Stolte, S.; Burszta-Adamiak, E. Treatment of electropolishing industrial wastewater and its impact on the immobilisation of *Daphnia magna*. *Environ. Res.* **2022**, *212*, 113438. [[CrossRef](#)]
5. Ramutshatsha-Makhwedzha, D.; Mavhungu, A.; Moropeng, M.L.; Mbaya, R. Activated carbon derived from waste orange and lemon peels for the adsorption of methyl orange and methylene blue dyes from wastewater. *Heliyon* **2022**, *8*, e09930. [[CrossRef](#)]
6. Jing, X.; Yuan, J.; Cai, D.; Li, B.; Hu, D.; Li, J. Concentrating and recycling of high-concentration printing and dyeing wastewater by a disc tube reverse osmosis-Fenton oxidation/low temperature crystallization process. *Sep. Purif. Technol.* **2021**, *266*, 118583. [[CrossRef](#)]
7. Tu, Y.; Shao, G.; Zhang, W.; Chen, J.; Qu, Y.; Zhang, F.; Tian, S.; Zhou, Z.; Ren, Z. The degradation of printing and dyeing wastewater by manganese-based catalysts. *Sci. Total Environ.* **2022**, *828*, 154390. [[CrossRef](#)]
8. Hao, J.; Ji, L.; Li, C.; Hu, C.; Wu, K. Rapid, efficient and economic removal of organic dyes and heavy metals from wastewater by zinc-induced in-situ reduction and precipitation of graphene oxide. *J. Taiwan Inst. Chem. E* **2018**, *88*, 137–145. [[CrossRef](#)]
9. Ye, X.; Wu, L.; Zhu, M.; Wang, Z.; Huang, Z.; Wang, M. Lotus pollen-derived hierarchically porous carbons with exceptional adsorption performance toward Reactive Black 5: Isotherms, kinetics and thermodynamics investigations. *Sep. Purif. Technol.* **2022**, *300*, 121899. [[CrossRef](#)]
10. Huang, W.; Wu, R.; Chang, J.; Juang, S.; Lee, D. Pristine and manganese ferrite modified biochars for copper ion adsorption: Type-wide comparison. *Bioresour. Technol.* **2022**, *360*, 127529. [[CrossRef](#)]
11. Liu, B.; Chen, T.; Wang, B.; Zhou, S.; Zhang, Z.; Li, Y.; Pan, X.; Wang, N. Enhanced removal of Cd²⁺ from water by AHP-pretreated biochar: Adsorption performance and mechanism. *J. Hazard. Mater.* **2022**, *438*, 129467. [[CrossRef](#)] [[PubMed](#)]
12. Tian, X.; Han, B.; Liang, J.; Yang, F.; Zhang, K. Tracking antibiotic resistance genes (ARGs) during earthworm conversion of cow dung in northern China. *Ecotox. Environ. Saf.* **2021**, *222*, 112538. [[CrossRef](#)] [[PubMed](#)]
13. Li, K.; Yang, Z.; Zhang, Y.; Li, Y.; Lu, L.; Niu, D. Effect of pretreated cow dung fiber on mechanical and shrinkage properties of cementitious composites. *J. Clean. Prod.* **2022**, *348*, 131374. [[CrossRef](#)]
14. Dang, Q.; Zhao, X.; Yang, T.; Gong, T.; He, X.; Tan, W.; Xi, B. Coordination of bacterial biomarkers with the dominant microbes enhances triclosan biodegradation in soil amended with food waste compost and cow dung compost. *Sci. Total Environ.* **2022**, *824*, 153837. [[CrossRef](#)] [[PubMed](#)]
15. Malolan, R.; Jayaraman, R.S.; Adithya, S.; Arun, J.; Gopinath, K.P.; SundarRajan, P.; Nasif, O.; Kim, W.; Govarthan, M. Anaerobic digestate water for *Chlorella pyrenoidosa* cultivation and employed as co-substrate with cow dung and chicken manure for methane and hydrogen production: A closed loop approach. *Chemosphere* **2021**, *266*, 128963. [[CrossRef](#)]
16. Sfez, S.; Meester, S.D.; Dewulf, J. Co-digestion of rice straw and cow dung to supply cooking fuel and fertilizers in rural India: Impact on human health, resource flows and climate change. *Sci. Total Environ.* **2017**, *609*, 1600–1615. [[CrossRef](#)]
17. Ma, Y.; Wu, S.; Zhuang, J.; Tong, J.; Qi, H. Tribological and physio-mechanical characterization of cow dung fibers reinforced friction composites: An effective utilization of cow dung waste. *Tribol. Int.* **2019**, *131*, 200–211. [[CrossRef](#)]
18. Yao, Q.; Qu, H.; Guo, Y.; Zhao, Z.; Qiao, L.; Wu, H.; Dong, A.; Liu, Y. Capturing copper on cow dung-based biochar adsorbents for reuse in water bacterial decontamination. *Colloid. Interfac. Sci.* **2021**, *45*, 100515. [[CrossRef](#)]
19. Hou, S.; Jia, S.; Jia, J.; He, Z.; Li, G.; Zuo, Q.; Zhuang, H. Fe₃O₄ nanoparticles loading on cow dung based activated carbon as an efficient catalyst for catalytic microbubble ozonation of biologically pretreated coal gasification wastewater. *J. Environ. Manag.* **2020**, *267*, 110615. [[CrossRef](#)]

20. Ramalingam, R.J.; Sivachidambaram, M.; Vijaya, J.J.; Al-Lohedan, H.A.; Muthumareeswaran, M.R. Synthesis of porous activated carbon powder formation from fruit peel and cow dung waste for modified electrode fabrication and application. *Biomass. Bioenerg.* **2020**, *142*, 105800. [[CrossRef](#)]
21. Chen, S.; Xia, Y.; Zhang, B.; Chen, H.; Chen, G.; Tang, S. Disassembly of lignocellulose into cellulose, hemicellulose, and lignin for preparation of porous carbon materials with enhanced performances. *J. Hazard. Mater.* **2021**, *408*, 124956. [[CrossRef](#)] [[PubMed](#)]
22. Chen, S.; Chen, G.; Chen, H.; Sun, Y.; Yu, X.; Su, Y.; Tang, S. Preparation of porous carbon-based material from corn straw via mixed alkali and its application for removal of dye. *Colloids Surf. A Physicochem. Eng. Asp.* **2019**, *568*, 173–183. [[CrossRef](#)]
23. Chen, S.; Wang, Z.; Xia, Y.; Zhang, B.; Chen, H.; Chen, G.; Tang, S. Porous carbon material derived from fungal hyphae and its application for the removal of dye. *RSC Adv.* **2019**, *9*, 25480. [[CrossRef](#)] [[PubMed](#)]
24. Chen, S.; Zhang, B.; Xia, Y.; Chen, H.; Chen, G.; Tang, S. Influence of mixed alkali on the preparation of edible fungus substrate porous carbon material and its application for the removal of dye. *Colloids Surf. A Physicochem. Eng. Asp.* **2021**, *609*, 125675. [[CrossRef](#)]
25. Zhang, B.; Jin, Y.; Qi, J.; Chen, H.; Chen, G.; Tang, S. Porous carbon materials based on *Physalis alkekengi* L. husk and its application for removal of malachite green. *Environ. Technol. Innov.* **2021**, *21*, 101343. [[CrossRef](#)]
26. Xia, Y.; Jin, Y.; Qi, J.; Chen, H.; Chen, G.; Tang, S. Preparation of biomass carbon material based on *Fomes fomentarius* via alkali activation and its application for the removal of brilliant green in wastewater. *Environ. Technol. Innov.* **2021**, *23*, 101659. [[CrossRef](#)]
27. Zhu, W.; Li, Y.; Dai, L.; Li, J.; Li, X.; Li, W.; Duan, T.; Lei, J.; Chen, T. Bioassembly of fungal mycelium/carbon nanotubes composite as a versatile adsorbent for water pollution control. *Chem. Eng. J.* **2018**, *339*, 214–222. [[CrossRef](#)]
28. Kharrazi, S.; Mirghaffari, N.; Dastgerdi, M.; Soleimani, M. A novel post-modification of powdered activated carbon prepared from lignocellulosic waste through thermal tension treatment to enhance the porosity and heavy metals adsorption. *Powder Technol.* **2020**, *366*, 358–368. [[CrossRef](#)]
29. Jin, Y.; Zhang, B.; Chen, G.; Chen, H.; Tang, S. Combining biological and chemical methods to disassemble of cellulose from corn straw for the preparation of porous carbons with enhanced adsorption performance. *Int. J. Biol. Macromol.* **2022**, *209*, 315–329. [[CrossRef](#)]
30. Pajda, M.; Wesełucha-Birczynska, A.; Kołodziej, A.; Swietek, M.; Długon, E.; Ziabka, M.; Błazewicz, M. A correlation of Raman data with the nanomechanical results of polymer nanomaterials with carbon nanoparticles. *J. Mol. Struct.* **2022**, *1264*, 133305. [[CrossRef](#)]
31. Zhang, B.; Jin, Y.; Huang, X.; Tang, S.; Chen, H.; Su, Y.; Yu, X.; Chen, S.; Chen, G. Biological self-assembled hyphae/starch porous carbon composites for removal of organic pollutants from water. *Chem. Eng. J.* **2022**, *450*, 138264. [[CrossRef](#)]
32. Chen, Z.; Wu, Y.; Huang, Y.; Song, L.; Chen, H.; Zhu, S.; Tang, C. Enhanced adsorption of phosphate on orange peel-based biochar activated by Ca/Zn composite: Adsorption efficiency and mechanisms. *Colloids Surf. A Physicochem. Eng. Asp.* **2022**, *651*, 129728. [[CrossRef](#)]
33. Mao, W.; Liu, J.; Yin, B.; Miao, S.; Li, Y.; Kong, D.; Wang, F. Co-Cr composite oxides efficiently catalyzed transfer hydrogenation of α , β -unsaturated aldehydes via N-doped carbon and interfacial electron migration. *Mol. Catal.* **2022**, *524*, 112257. [[CrossRef](#)]
34. Qiao, X.; Xia, Y.; Su, X.; Wang, B.; Chen, G.; Chen, H. Preparation of biomass carbon material based on fulvic acid and its application in dye and antibiotic treatments. *Colloids Surf. A Physicochem. Eng. Asp.* **2022**, *638*, 128302. [[CrossRef](#)]
35. Gao, W. Porous biomass carbon derived from *Clivia miniata* leaves via NaOH activation for removal of dye. *Materials* **2022**, *15*, 1285. [[CrossRef](#)]
36. Liang, D.; Tian, X.; Zhang, Y.; Zhu, G.; Gao, Q.; Liu, J.; Yu, X. A weed-derived hierarchical porous carbon with a large specific surface area for efficient dye and antibiotic removal. *Int. J. Mol. Sci.* **2022**, *23*, 6146. [[CrossRef](#)]
37. Rodríguez-López, M.I.; Pellicer, J.A.; Gómez-Morte, T.; Auñón, D.; Gómez-López, V.M.; Yáñez-Gascón, M.J.; Gil-Izquierdo, Á.; Cerón-Carrasco, J.P.; Crini, G.; Núñez-Delicado, E.; et al. Removal of an Azo dye from wastewater through the use of two technologies: Magnetic cyclodextrin polymers and pulsed light. *Int. J. Mol. Sci.* **2022**, *23*, 8406. [[CrossRef](#)]
38. Cai, Z.; Liu, Q.; Li, H.; Wang, J.; Tai, G.; Wang, F.; Han, J.; Zhu, Y.; Wu, G. Waste-to-resource strategy to fabricate functionalized MOFs composite material based on durian shell biomass carbon fiber and Fe₃O₄ for highly efficient and recyclable dye adsorption. *Int. J. Mol. Sci.* **2022**, *23*, 5900. [[CrossRef](#)]
39. Luna, M.S.; Greco, F.; Pastore, R.; Mensitieri, G.; Filippone, G.; Aprea, P.; Mallamace, D.; Mallamace, F.; Chen, S. Tailoring Chitosan/LTA Zeolite hybrid aerogels for anionic and cationic dye adsorption. *Int. J. Mol. Sci.* **2021**, *22*, 5535. [[CrossRef](#)]
40. Delpiano, G.R.; Tocco, D.; Medda, L.; Magner, E.; Salis, A. Adsorption of Malachite Green and Alizarin Red S dyes using Fe-BTC metal organic framework as adsorbent. *Int. J. Mol. Sci.* **2021**, *22*, 788. [[CrossRef](#)]
41. Hamedi, A.; Trotta, F.; Zarandi, M.B.; Zanetti, M.; Caldera, F.; Anceschi, A.; Nateghi, M.R. In situ synthesis of MIL-100(Fe) at the surface of Fe₃O₄@AC as highly efficient dye adsorbing nanocomposite. *Int. J. Mol. Sci.* **2019**, *20*, 5612. [[CrossRef](#)] [[PubMed](#)]
42. Guo, Y.; Yan, C.; Wang, P.; Rao, L.; Wang, C. Doping of carbon into boron nitride to get the increased adsorption ability for tetracycline from water by changing the pH of solution. *Chem. Eng. J.* **2020**, *387*, 124136. [[CrossRef](#)]
43. Ndagijimana, P.; Liu, X.; Yu, G.; Wang, Y. Synthesis of a novel core-shell-structure activated carbon material and its application in sulfamethoxazole adsorption. *J. Hazard. Mater.* **2019**, *368*, 602–612.
44. Blanco-Martínez, D.; Giraldo, L.; Moreno-Piraján, J. Effect of the pH in the adsorption and in the immersion enthalpy of monohydroxylated phenols from aqueous solutions on activated carbons. *J. Hazard. Mater.* **2009**, *169*, 291–296. [[CrossRef](#)] [[PubMed](#)]

45. Mane, V.; Babu, P. Studies on the adsorption of Brilliant Green dye from aqueous solution onto low-cost NaOH treated saw dust. *Desalination* **2011**, *273*, 321–329. [[CrossRef](#)]
46. Liu, K.; Li, H.; Wang, Y.; Gou, X.; Duan, Y. Adsorption and removal of rhodamine B from aqueous solution by tannic acid functionalized graphene. *Colloid. Surf. A* **2015**, *477*, 35–41. [[CrossRef](#)]
47. Koniarz, M.P.; Goscianska, J.; Pietrzak, R. Adsorption of dyes on the surface of polymer nanocomposites modified with methylamine and copper(II) chloride. *J. Colloid Interf. Sci.* **2017**, *504*, 549–560. [[CrossRef](#)]
48. Anandkumar, J.; Mandal, B. Adsorption of chromium(VI) and Rhodamine B by surface modified tannery waste: Kinetic, mechanistic and thermodynamic studies. *J. Hazard. Mater.* **2011**, *186*, 1088–1096. [[CrossRef](#)]
49. Hayeeye, F.; Sattar, M.; Chinpa, W.; Sirichote, O. Kinetics and thermodynamics of Rhodamine B adsorption by gelatin/activated carbon composite beads. *Colloid. Surface. A* **2017**, *513*, 259–266. [[CrossRef](#)]
50. Gad, H.M.H.; El-Sayed, A.A. Activated carbon from agricultural by-products for the removal of Rhodamine-B from aqueous solution. *J. Hazard. Mater.* **2009**, *168*, 1070–1081. [[CrossRef](#)]
51. Yu, J.; Li, B.; Sun, X.; Yuan, J.; Chi, R. Polymer modified biomass of baker's yeast for enhancement adsorption of methylene blue, rhodamine B and basic magenta. *J. Hazard. Mater.* **2009**, *168*, 1147–1154. [[CrossRef](#)] [[PubMed](#)]
52. Li, L.; Liu, S.; Zhu, T. Application of activated carbon derived from scrap tires for adsorption of Rhodamine B. *J. Environ. Sci-China* **2010**, *22*, 1273–1280. [[CrossRef](#)]
53. Tuzen, M.; Sari, A.; Saleh, T.A. Response surface optimization, kinetic and thermodynamic studies for effective removal of rhodamine B by magnetic AC/CeO₂ nanocomposite. *J. Environ. Manage.* **2018**, *206*, 170–177. [[CrossRef](#)]
54. Huang, Y.; Zheng, X.; Feng, S.; Guo, Z.; Liang, S. Enhancement of rhodamine B removal by modifying activated carbon developed from *Lythrum salicaria* L. with pyruvic acid. *Colloid. Surface. A* **2016**, *489*, 154–162. [[CrossRef](#)]
55. Zhang, T.; Huang, J. N-vinylimidazole modified hyper-cross-linked resins and their adsorption toward Rhodamine B: Effect of the cross-linking degree. *J. Taiwan Inst. Chem. E.* **2017**, *80*, 293–300. [[CrossRef](#)]
56. Ding, L.; Zou, B.; Gao, W.; Liu, Q.; Wang, Z.; Guo, Y.; Wang, X.; Liu, Y. Adsorption of Rhodamine-B from aqueous solution using treated rice husk-based activated carbon. *Colloid. Surface. A* **2014**, *446*, 1–7. [[CrossRef](#)]
57. Mittal, B.H.; Mishra, S.B. Gum ghatti and Fe₃O₄ magnetic nanoparticles based nanocomposites for the effective adsorption of rhodamine B. *Carbohydr. Polym.* **2014**, *101*, 1255–1264. [[CrossRef](#)]
58. Inyinbor, A.A.; Adekola, F.A.; Olatunji, G.A. Kinetics, isotherms and thermodynamic modeling of liquid phase adsorption of Rhodamine B dye onto *Raphia hookeri* fruit epicarp. *Water Resour. Ind.* **2016**, *15*, 14–27. [[CrossRef](#)]
59. Chen, S.; Tang, S.; Sun, Y.; Wang, G.; Chen, H.; Yu, X.; Su, Y.; Chen, G. Preparation of a highly porous carbon material based on quinoa husk and its application for removal of dyes by adsorption. *Materials* **2018**, *11*, 1407. [[CrossRef](#)]
60. Chen, Y.; Wang, F.; Duan, L.; Yang, H.; Gao, J. Tetracycline adsorption onto rice husk ash, an agricultural waste: Its kinetic and thermodynamic studies. *J. Mol. Liq.* **2016**, *222*, 487–494. [[CrossRef](#)]
61. Premarathna, K.S.D.; Rajapaksha, A.U.; Adassoriya, N.; Sarkar, B.; Sirimuthu, N.M.S.; Cooray, A.; Ok, Y.S.; Vithanage, M. Clay-biochar composites for sorptive removal of tetracycline antibiotic in aqueous media. *J. Environ. Manage.* **2019**, *238*, 315–322. [[CrossRef](#)] [[PubMed](#)]
62. Yu, H.; Gu, L.; Chen, L.; Wen, H.; Zhang, D.; Tao, H. Activation of grapefruit derived biochar by its peel extracts and its performance for tetracycline removal. *Bioresour. Technol.* **2020**, *316*, 123971. [[CrossRef](#)] [[PubMed](#)]
63. Huang, H.; Niu, Z.; Shi, R.; Tang, J.; Lv, L.; Wang, J.; Fan, Y. Thermal oxidation activation of hydrochar for tetracycline adsorption: The role of oxygen concentration and temperature. *Bioresour. Technol.* **2020**, *306*, 123096. [[CrossRef](#)] [[PubMed](#)]
64. Zhang, D.; He, Q.; Hu, X.; Zhang, K.; Chen, C.; Xue, Y. Enhanced adsorption for the removal of tetracycline hydrochloride (TC) using ball-milled biochar derived from crayfish shell. *Colloid. Surf. A* **2021**, *615*, 126254. [[CrossRef](#)]
65. Xiang, W.; Wan, Y.; Zhang, X.; Tan, Z.; Xia, T.; Zheng, Y.; Gao, B. Adsorption of tetracycline hydrochloride onto ball-milled biochar: Governing factors and mechanisms. *Chemosphere* **2020**, *255*, 127057. [[CrossRef](#)]
66. Oladipo, A.A.; Ifebajo, A.O. Highly efficient magnetic chicken bone biochar for removal of tetracycline and fluorescent dye from wastewater: Two-stage adsorber analysis. *J. Environ. Manage.* **2018**, *209*, 9–16. [[CrossRef](#)]
67. Zhou, Y.; He, Y.; He, Y.; Liu, X.; Xu, B.; Yu, J.; Dai, C.; Huang, A.; Pang, Y.; Luo, L. Analyses of tetracycline adsorption on alkali-acid modified magnetic biochar: Site energy distribution consideration. *Sci. Total Environ.* **2019**, *650*, 2260–2266. [[CrossRef](#)]
68. Miao, J.; Wang, F.; Chen, Y.; Zhu, Y.; Zhou, Y.; Zhang, S. The adsorption performance of tetracyclines on magnetic graphene oxide: A novel antibiotics absorbent. *Appl. Surf. Sci.* **2019**, *475*, 549–558. [[CrossRef](#)]
69. Yang, Z.; Zhao, Z.; Yang, X.; Ren, Z. Xanthate modified magnetic activated carbon for efficient removal of cationic dyes and tetracycline hydrochloride from aqueous solutions. *Colloid. Surface. A* **2021**, *615*, 126273. [[CrossRef](#)]
70. Gao, Y.; Li, Y.; Zhang, L.; Huang, H.; Hu, J.; Shah, S.M.; Su, X. Adsorption and removal of tetracycline antibiotics from aqueous solution by graphene oxide. *J. Colloid Interf. Sci.* **2012**, *368*, 540–546. [[CrossRef](#)]
71. Martins, A.; Pezoti, O.; Cazetta, A.; Bedin, K.; Yamazaki, D.; Bandoch, G.; Asefa, T.; Visentainer, J.; Almeida, V. Removal of tetracycline by NaOH-activated carbon produced from macadamia nut shells: Kinetic and equilibrium studies. *Chem. Eng. J.* **2015**, *260*, 291–299. [[CrossRef](#)]
72. Yang, G.; Gao, Q.; Yang, S.; Yin, S.; Cai, X.; Yu, X.; Zhang, S.; Fang, Y. Strong adsorption of tetracycline hydrochloride on magnetic carbon-coated cobalt oxide nanoparticles. *Chemosphere* **2020**, *239*, 124831. [[CrossRef](#)] [[PubMed](#)]

73. Chen, Y.; Liu, J.; Zeng, Q.; Liang, Z.; Ye, X.; Lv, Y.; Liu, M. Preparation of *Eucommia ulmoides* lignin-based high-performance biochar containing sulfonic group: Synergistic pyrolysis mechanism and tetracycline hydrochloride adsorption. *Bioresour. Technol.* **2021**, *329*, 124856. [[CrossRef](#)] [[PubMed](#)]
74. Masoumi, S.; Tabrizi, F.F.; Sardarian, A.R. Efficient tetracycline hydrochloride removal by encapsulated phosphotungstic acid (PTA) in MIL-53 (Fe): Optimizing the content of PTA and recycling study. *J. Environ. Chem. Eng.* **2020**, *8*, 103601. [[CrossRef](#)]